CO$_2$ Bubble Nucleation in Polystyrene: Experimental and Modeling Studies

Zhihua Guo, Adam C. Burley, Kurt W. Koelling, Isamu Kusaka, L. James Lee, David L. Tomasko

William G. Lowrie Department of Chemical and Biomolecular Engineering, The Ohio State University, Columbus, Ohio 43210

ABSTRACT: Polymer foams are used extensively in a variety of applications. A firm understanding of bubble nucleation is vital to predict foam properties based on process conditions. However, a number of theoretical and experimental challenges have thus far limited progress in this area. We propose the use of a scaling theory to connect nucleation behavior to well understood bulk phase behavior of polystyrene-CO$_2$ systems, which can be predicted by equations of state, such as the Sanchez–Lacombe equation of state. Scaling theory of nucleation asserts that when the reversible work of critical nucleus formation is properly normalized and plotted against the normalized degree of supersaturation, the resulting scaling curve is insensitive to temperature and the materials being used. Once the form of the scaling function is known, it can be used to predict the nucleation barrier knowing only the initial foaming conditions and calculating only bulk thermodynamic values. Using an extension of diffuse interface theory, we determined the slope of the scaling curve near saturation. This initial slope allows us to constrain the scaling function for better predictions of the reversible work. We also performed a series of experiments to help verify the accuracy of the scaling theory. The scaled free energy barriers determined from our experiments are consistent with the scaling function so constructed, and our theoretical results qualitatively agree with those found previously. © 2012 Wiley Periodicals, Inc. J Appl Polym Sci 125: 2170–2186, 2012

Key words: nucleation; polystyrene; foams; scaling function; diffuse interface theory

INTRODUCTION

Plastic foams are widely used in applications such as insulation, cushioning, shock- and sound-absorbents, packaging, and even scaffolds for cell attachment and growth.[1–4] A wide variety of polymers are used for foaming, including polyurethane (PU), polyisocyanurate, polystyrene (PS), polyolefin, poly(vinyl chloride) (PVC), and epoxies. According to the most recent US Economic Census, in 2007 the value of primary product shipments of PS foams was more than \$6.5 billion, accounting for roughly 40% of the total foams industry.[5] As one of the most versatile thermoplastic resins available for the production of low-cost plastic foams, PS is used in this study.

As chlorofluorocarbons (CFCs) and hydrochlorofluorocarbons (HCFCs) are being phased out according to the Montreal Protocol,[6] CO$_2$ has emerged as one of the most promising alternatives because it is environmentally safe, nontoxic, nonflammable, and inexpensive. Extensive research[7–12] has been carried out in polymer foaming with CO$_2$ in recent years. CO$_2$ is being explored for products ranging from low-density insulation ($<$0.04 g/cm^3) to high-density structural foams ($\sim$ 0.7 g/cm^3). However, CO$_2$ has its drawbacks, such as low solubility and high diffusivity in comparison with other blowing agents. Therefore, CO$_2$ sometimes leads to foams with higher density and/or poor surface quality, and almost always requires higher operating pressures than other agents. Currently, nanoparticles are being studied as additives to overcome these problems.[13–15] Another approach is to use polymer blends.[16–20]

The changes in foam quality and properties resulting from the use of alternative blowing agents requires modification of existing foaming processes and protocols, particularly with regard to operating conditions. However, the underlying nucleation phenomenon is not well understood and thus a rational approach to this transition based on a fundamental consideration is not possible. In light of the extensive retooling of industrial processes necessary to accommodate the use of CO$_2$ and other more environmentally benign blowing agents, a fundamental understanding of nucleation phenomena is crucial.

The most widely used method of producing foams by a physical blowing agent involves saturating the

polymer phase with blowing agent and triggering bubble nucleation and growth by a sudden pressure drop. In general, the foaming process comprises three fundamental steps: bubble nucleation, bubble growth, and bubble stabilization.[21] During bubble nucleation, an embryo of the new gas phase forms in a metastable melt phase, requiring an activation energy barrier to be surmounted.

Bubble nucleation plays a key role in the foaming process. However, bubble nucleation is a complex process that is challenging for both experimental and theoretical studies. Therefore, a coherent theoretical approach, supplemented by data from careful experiments, is needed. In this study, we have explored the use of a scaling approach to predict nucleation behavior from phase diagrams and bulk thermodynamic quantities. This scaling approach utilizes the classical nucleation theory (CNT) as a basis for obtaining scaled values. We have then used results from experiments to attempt to validate the theoretical predictions.

THEORETICAL BACKGROUND

Although a variety of theoretical models[22] have been proposed during the past few decades, CNT is still regarded as the most successful approach for quantitative prediction of nucleation phenomena.[23] It has also been used[24–32] widely to describe bubble nucleation in the polymer foaming process, though it is known to seriously under predict the bubble nucleation events in polymer processing.[29]

In CNT, the steady state nucleation rate, defined as the number of critical nuclei formed per unit time in a unit volume of the parent phase, is given by[33,34]

$$J_{ss} = J_0 e^{-W/k_B T}, \qquad (1)$$

where W is the reversible work of critical nucleus formation, k_B is the Boltzmann factor, and T is the absolute temperature. J_0 follows from a kinetic consideration of the bubble formation process, and is given by[35]

$$J_0 = N \left(\frac{2\gamma}{\pi m B} \right)^{1/2}, \qquad (2)$$

where the prefactor N is the number density of the blowing agent molecule in polymer–blowing agent solutions,[27,29] m is the mass of the gas molecule, and γ is the interfacial tension between the metastable parent phase and the nucleating phase. B is a dimensionless factor that varies in value between 2/3 and 1, depending primarily upon the viscosity of the material. Since fairly long relaxation times are expected in a polymer, B is considered to have a value of 1 for this study.[35]

Since W appears in the exponent of eq. (1), it has a larger impact on the value of the nucleation rate and its accurate calculation is considered more essential than that of J_0. Gibbs derived the exact expression for W[36]:

$$W = \frac{16\pi\gamma^3}{3(\Delta P)^2}, \qquad (3)$$

where $\Delta P = P^\beta - P^\alpha$, wherein P^α is the pressure of the metastable phase (α) and P^β is the pressure of the nucleating phase (β) if it existed in bulk at the same temperature and chemical potential as the metastable phase α.[36,37] We note that P^β is computed from the uniformity of temperature and chemical potentials using the equation of state of bulk gas phase, i.e., without considering the effect of the interface. To stress this, bulk β phase is often referred to as the reference or the hypothetical bulk phase.[38] Accordingly, we refer to P^β as the hypothetical vapor pressure.

Direct application of eq. (3) is very difficult, if not impossible, because the value of γ depends on the size of the critical nucleus and is experimentally inaccessible. Accordingly, CNT introduces an approximation by replacing γ with the macroscopic interfacial tension of the flat interface, γ_∞, which is experimentally accessible:

$$W^{cl} = \frac{16\pi\gamma^3_\infty}{3(\Delta P)^2}. \qquad (4)$$

The calculation of the reversible work of nucleation using this expression will bring significant error. In fact, thermodynamic considerations demand that both W and γ vanish at the spinodal,[39] while W^{cl} does not. The scaling theory discussed below may provide a connection between W and W^{cl} that will lead to a better prediction of W through calculation of W^{cl}. It should be noted also that the measurement of macroscopic interfacial tension, γ_∞, is still difficult for polymer–gas systems because of the high viscosity and rheological characteristics of polymers.[40]

To overcome the shortcomings of classical theory, many researchers have made efforts to understand nucleation at a molecular level by using computer simulation[41] and statistical mechanical density functional theory (DFT),[42] for example. However, their ability to make quantitative predictions is still very limited. Accordingly, many researchers have also pursued more phenomenological approaches. For instance, Gránásy[43,44] proposed the diffuse interface theory (DIT) for vapor condensation and crystal nucleation. Recently, it was extended to bubble nucleation.[45]

McGraw and Laaksonen[46] made important progress by proposing the scaling hypothesis, which states that the difference between W^{cl} and W is only a function of temperature. When combined with the

boundary conditions $W/W^{cl} = 1$ at saturation and $W/W^{cl} = 0$ at the spinodal, the hypothesis leads to[47]:

$$W/_{W^{cl}} = 1 - \xi^2, \qquad (5)$$

where ξ is some normalized degree of supersaturation.

From eqs. (3) and (4), the scaled free energy barrier is defined as:

$$\phi(\xi) = \frac{W}{W^{cl}} = \left(\frac{\gamma}{\gamma_\infty}\right)^3. \qquad (6)$$

Two thermodynamic boundary conditions should hold. As previously discussed, W should vanish at the spinodal, and hence $\phi = 0$ at $\xi = 1$. Also, $\phi = 1$ when $\xi = 0$ since $\gamma = \gamma_\infty$ at saturation ($\xi = 0$).

In contrast to eq. (5), the slope of W/W^{cl} at $\xi = 0$ is nonzero in general. Thus, an alternative scaling function with nonzero initial slope (slope at $\xi = 0$) is expected to provide a better prediction of W/W^{cl}. We calculated this slope using an extension of DIT, which we develop here for a binary system. The major advantage of this approach rests on the fact that DIT only uses bulk thermodynamic quantities and does not require more involved molecular level theories.

EXPERIMENTAL BACKGROUND

The accurate measurement of nucleation is still a significant challenge. A variety of devices and methods have been developed to investigate homogeneous gas-to-liquid nucleation and a number of chemical compounds have been studied (see Iland et al.[48] for an overview of different methods and their measurement ranges). In contrast, literature for the measurement of bubble nucleation is rare. In one of the few experimental measurements of homogeneous bubble nucleation rate, Strey and coworkers[49] have extended the nucleation-pulse method to measure the nucleation rate as a function of supersaturation in gas-saturated liquids at constant temperature.

Han and Han[28,29] studied bubble nucleation in concentrated polymeric solutions (40, 50, and 60 wt % PS in the blowing agent toluene with two initial pressures, 400 and 600 psi) using laser light scattering (i.e., CAMS). A great deal of bubble nucleation and growth information was obtained in their study, including the critical bubble size and the total number of bubbles nucleated. However, this method is difficult to extend to foaming systems where the blowing agent only has a small solubility in the polymer matrix, such as CO_2 in PS.

A large number of publications present intriguing conclusions about foaming behavior. They usually assume each nucleation site produces a bubble, no bubble coalescence occurs, and every bubble that has nucleated grows to a detectable size. The number of bubbles in a two-dimensional cross-section of the sample can be counted, from which one can extrapolate bubble nucleation rate. Colton and Suh[24] were among the earliest to study nucleation by this method. Recently, several researchers obtained bubble nucleation and growth rate data in the polymer foaming process using the same method. Taki et al.[50,51] conducted in situ visual observations for batch foaming processes of polypropylene (PP) and PP-clay nanocomposites with CO_2 to understand bubble nucleation and growth in the early stages. They developed a high-pressure autoclave that has two sapphire windows in the walls. A high-speed digital camera with a microscope was used to observe the behavior. Guo et al.[52] used a similar experimental setup but a much higher speed camera to study microcellular foaming with a higher pressure drop and a maximum achievable pressure drop rate of 2.5 GPa/s. However, in these studies, the sample touched the sapphire windows, possibly inducing heterogeneous nucleation. Nevertheless, these data are the only available data on bubble nucleation rates in PS-CO_2 systems and will be used below for comparison.

THEORETICAL METHOD

In constructing the scaling function, both the binodal (on which $\xi = 0$) and the spinodal (on which $\xi = 1$) curves need to be known. Experimental data for spinodal curves for polymer–diluent systems are very scarce. Kiran[53] and his coworkers used time- and angle-resolved light scattering techniques to map out the binodal and spinodal envelopes of some systems, such as PDMS-CO_2. However, for those systems in which the gas has a low affinity with the polymer, such as PS-CO_2, the data are nonexistent.

Therefore, we use equations of state (EOS) to predict the phase boundaries, which is a common practice. At a given temperature, the binodal curve is determined by finding the composition that upholds the equality of the chemical potential of CO_2 in both phases for various values of pressure. The spinodal curve defines the limit of metastability of a homogeneous phase,[54] and is determined by a locus of points where the second composition derivative of the free energy vanishes. In our study, we were especially interested in the region where the mass fraction of polymer is much larger than that of the foaming agent, CO_2.

The Sanchez–Lacombe (S–L) EOS[55–59] was used to determine the phase diagram and to predict other thermodynamic quantities. The S–L EOS is widely used in phase equilibria calculation in polymer–solvent systems.[60–63] It has also been used to predict thermodynamic quantities, such as entropy.[59]

With known initial and final pressures, such as from the pressure drop of a nucleation experiment at a certain temperature, ΔP can be calculated by the S–L EOS. The final pressure corresponds to P^α. P^β is then identified as the pressure at which the hypothetical vapor phase has the same chemical potential of CO_2 as that in the mixture at P^α. Similarly, we can calculate ΔP_s, which is the value of ΔP calculated at the spinodal. The normalized degree of supersaturation, ξ, may then be defined as the ratio of these two quantities, $\xi = \Delta P / \Delta P_s$. If these calculations are done for a series of values of ξ at which experiments have been performed and if the corresponding scaled free energy barrier, $\phi(\xi) = W/W^{cl}$, is known for these experiments, a scaling curve can be constructed.

Alternatively, if the initial slope of $\phi(\xi)$, i.e. $(\partial\phi/\partial\xi)_{\xi=0}$, can be estimated, we may be able to predict a reasonably accurate scaling function without relying heavily on experiments. We use DIT for this purpose.

The extension of DIT to multi-component systems is fairly straightforward. The derivation closely follows that of Ref. 45 and intermediate details are available in Appendix A. In this article, we restrict our attention to the case of bubble nucleation. Beginning from an equation equivalent to eq. (24) of this reference, we note that the reversible work to form a critical nucleus in a metastable liquid phase of volume $v(\bar{r})$ at fixed temperature T and chemical potentials μ_i may be written as:

$$W = \int_v \left[\omega(\bar{r}) - \omega^l\right] d\bar{r}, \tag{7}$$

where ω is the grand potential per unit volume. For an inhomogeneous system,

$$\omega(\bar{r}) = \rho(\bar{r})\left[u_N(\bar{r}) - Ts_N(\bar{r}) - \sum_i \mu_i x_i(\bar{r})\right], \tag{8}$$

where ρ is the total number density of molecules, u_N is the internal energy per molecule, s_N is the entropy per molecule, μ_i is the chemical potential of each component, and x_i is the mole fraction of each component. In the homogeneous liquid phase, this equation becomes:

$$\omega^l = \rho^l\left[u_N^l - Ts_N^l - \sum_i \mu_i x_i^l\right] = -P^l. \tag{9}$$

From eqs. (8) and (9), we obtain:

$$\omega(\bar{r}) - \omega^l = \Delta\chi(\bar{r}) - T\Delta s(\bar{r}), \tag{10}$$

where

$$\Delta\chi(\bar{r}) := \rho(\bar{r})\left\{u_N(\bar{r}) - u_N^l - \sum_i \mu_i[x_i(\bar{r}) - x_i^l] + P^l\left[\frac{1}{\rho(\bar{r})} - \frac{1}{\rho^l}\right]\right\}$$

$$\Delta s(\bar{r}) := \rho(\bar{r})\lfloor s_N(\bar{r}) - s_N^l\rfloor.$$

In this formulation, $\Delta\chi$ and Δs are the enthalpy and entropy distributions per volume, respectively, in the system. Applying eq. (10) to the homogeneous hypothetical pure vapor phase having the same temperature and chemical potential (of the pure species) as the liquid phase, we get:

$$\omega^v - \omega^l = \Delta\chi^v - T\Delta s^v = -\Delta P^v \tag{11}$$

where

$$\Delta\chi^v := \rho^v\left[u_N^v - u_N^l - \sum_i \mu_i(x_i^v - x_i^l) + P^l\left(\frac{1}{\rho^v} - \frac{1}{\rho^l}\right)\right]$$

$$\Delta s^v := \rho^v(s_N^v - s_N^l).$$

$$\Delta P^v := P^v - P^l = -\Delta P^l. \tag{12}$$

It can then be shown that:

$$\Delta\chi^v = T\Delta s^v - \Delta P^v. \tag{13}$$

Note that $\Delta\chi$, Δs, and ΔP for the homogeneous liquid are defined by eq. (12) with the superscripts l and v exchanged.

Applying eq. (7) to a spherical interface, we find:

$$W = 4\pi \int_0^{+\infty} \left[\omega(\bar{r}) - \omega^l\right] r^2 dr. \tag{14}$$

In DIT, we express W in reference to two dividing surfaces. Associated with each dividing surface is the surface excess quantity, which is defined as the difference in the extensive quantity (per unit area of the dividing surface) between the real system and the reference system composed entirely of two bulk phases without any interface (indicated by a sharp vertical transition).[64] Let R_s and R_χ denote the radii of the dividing surfaces for which the surface excess of Δs and $\Delta\chi$ vanish, respectively, and define $\delta_G := R_s - R_\chi$, the Gránásy length. Ref. 43 provides a helpful diagram of these definitions (see Figure 1 of Ref. 43). Then eq. (14) becomes:

$$W = -\frac{4\pi}{3}\left[\Delta\chi^l(R_s - \delta_G)^3 - T\Delta s^l R_s^3\right]. \tag{15}$$

If we ignore the possible dependence of δ_G on R_s (by assuming a sufficiently large bubble) and take the derivative of W with respect to R_s, we get:

$$\frac{\partial W}{\partial R_s} = 4\pi\Delta P\left[(R_s - \delta_G\zeta)^2 + \delta_G^2\zeta(1-\zeta)\right], \quad (16)$$

where

$$\zeta := -\frac{\Delta\chi^l}{\Delta P^l} = 1 - T\frac{\Delta s^l}{\Delta P^l}.$$

The radius R_s^* of the critical nucleus is determined by solving

$$\left.\frac{\partial W}{\partial R_s}\right|_{R_s = R_s^*} = 0.$$

Although $\Delta\chi^l < 0$ and $\Delta\chi^l > 0$ are both possible, the DIT framework demands that $\Delta\chi^l < 0$, as explained in Appendix A. For this case, $\zeta < 0$ and we find that the local maximum of W (for which $R_s = R_s^*$, where R_s^* is the critical radius) is given by:

$$R_s^* = \delta_G\zeta + \sqrt{\delta_G^2\zeta(\zeta - 1)} = \zeta(\delta_G - |\delta_G|q), \quad (17)$$

where $\quad q := \sqrt{1 - 1/\zeta}.$ (18)

Since $q > 1$, $R_s^* > 0$ is true irrespective of the sign of δ_G. However, as Appendix A notes, δ_G must always be negative for bubble nucleation. So,

$$R_s^* = \zeta\delta_G(1 + q) \quad (19)$$

and eq. (15) becomes:

$$W^* = -\frac{4\pi}{3}\left\{\Delta\chi^l[\zeta\delta_G(1+q) - \delta_G]^3 - T\Delta s^l[\zeta\delta_G(1+q)]^3\right\}. \quad (20)$$

Thus,

$$W^* = -\frac{4\pi}{3}\delta_G^3\Delta P^l\psi_G, \quad (21)$$

where we defined

$$\psi_G := \zeta(\zeta - 1)[2(1+q)\zeta - 1]. \quad (22)$$

Using eq. (13) of Ref. 45, eq. (4) can be rewritten as:

$$W^{cl} = \frac{16\pi\gamma_\infty^3}{3(\Delta P^l)^2} = \frac{16\pi\delta_{G0}^3 L_0^3}{3(\Delta P^l)^2}, \quad (23)$$

for vapor condensation, where $L_0 \equiv -T\Delta s_0^l = -\Delta\chi_0^l > 0$ and the subscript 0 indicates a quantity at phase coexistence. In vapor condensation it has been shown that δ_G and δ_{G0}, the Gránásy length for the flat interface, are both positive.[44,45,65] This means that $\Delta\chi$ penetrates the liquid deeper than Δs and thus $R_s > R_\chi > 0$. We expect that $\Delta\chi$ will still penetrate the liquid deeper in bubble nucleation.

However, the liquid and vapor phases are now reversed, so $R_\chi > R_s > 0$. This means that δ_G and the δ_{G0} used in eq. (23) have opposite sign. Using the approximation introduced by Gránásy[65] regarding the magnitude of δ_G, we conclude that $\delta_G \approx -\delta_{G0}$. Combining eqs. (21) and (23) and using this approximation, we finally obtain:

$$\phi = \frac{W}{W^{cl}} = \frac{1}{4}\left(\frac{\Delta P^l}{L_0}\right)^3\psi_G. \quad (24)$$

The DIT prediction quickly becomes inaccurate as the system moves away from saturation, but it should remain sufficiently accurate near saturation to allow for an accurate calculation of the initial slope.[45] Beginning from eq. (24) it can be shown that the derivative of ϕ with respect to ξ results in:

$$\left(\frac{\partial\phi}{\partial\xi}\right)_{\xi=0} = \frac{3\Delta P_s^l}{2L_0}\left[1 - 2T\left(\frac{\partial\Delta s^l}{\partial\Delta P^l}\right)\right]. \quad (25)$$

Further details on this derivation can be found in Appendix B. To apply this equation, the inner derivative must be evaluated numerically; for example, as a finite difference:

$$\left(\frac{\partial\Delta s^l}{\partial\Delta P^l}\right) = \frac{\Delta s_0^l - \Delta s^l}{0 - \Delta P^l}$$
$$= \frac{\rho_0^l\left(s_{N,0}^l - s_{N,0}^v\right) - \rho^l\left(s_{N,\alpha}^l - s_{N,\beta}^v\right)}{-\Delta P^l}, \quad (26)$$

where ρ_0^l and ρ^l are molecular number densities and s_N indicates entropy per molecule. Since this analysis inherently involves small changes from saturation, it can be assumed that $\rho_0^l \approx \rho^l$. Given temperature and a saturation pressure, the initial slope can now be determined for a certain mass fraction, using only bulk thermodynamic quantities, including the entropy.

In the S–L EOS, the entropy is given by[59,66]:

$$-\frac{S}{k_B rN} = \left(\tilde{v} - 1\right)\ln\left(1 - \tilde{\rho}\right) + \frac{\ln\tilde{\rho}}{r} + \sum\frac{\phi_i}{r_i}\ln\left(\frac{\phi_i}{r_i}\right) +$$
$$1 + \frac{\ln(2/z) - 1}{r} + \sum\left(\frac{\phi_i}{r_i}\right)(r_i - 2)\left[\ln(1 - f_i) - f_i\frac{\Delta\varepsilon_i}{k_BT}\right], \quad (27)$$

where z and $\Delta\varepsilon_i$ are the coordination number and the increase in intramolecular energy accounting for bond flexing, respectively, and f_i is a function of z and $\Delta\varepsilon_i$. Generally, z is chosen (a value of 10 is a typical choice) and then $\Delta\varepsilon_2$ is found for the polymer ($\Delta\varepsilon_1$ corresponds to CO_2 and is taken to be zero). The value of $\Delta\varepsilon_2$ that satisfies the Gibbs–Di Marzio criterion, i.e., that the entropy of the pure polymer be zero at the normal glass transition temperature,[59,67] is typically chosen. We found, however,

that if this criterion is followed, the entropy of the polymer mixture can be negative for certain temperatures and pressures, which is unphysical. To avoid this, we determined a range of $\Delta\varepsilon_2$ values for which the liquid entropy was positive and less than the vapor entropy at a specific temperature. We then chose the value of $\Delta\varepsilon_2$ that resulted in the scaling function in best agreement with the experimentally determined scaling curve. For this system, that value was $\Delta\varepsilon_2 = 9675$ J mol^{-1}.

EXPERIMENTAL METHOD

The PS (CX5197; $M_w = 187,000$, $M_n = 86,000$) was from Total Petrochemicals (formerly Atofina). The foaming agent, CO$_2$ (>99.9%), was provided by Praxair and used without further purification. PS plates were made by compression molding (170°C) and cut into samples with dimensions of 7 mm × 20 mm × 0.6 mm. This thickness was chosen because if the sample was too thick (e.g., >1 mm), it became difficult to count the number of bubbles by analyzing the images because there were bubbles behind the bubbles being counted in the viewing direction. On the other hand, if the sample was too thin (e.g., <0.4 mm), the sample warped under the experimental conditions, resulting in the sample moving out of the focal plane of the camera.

The experimental setup, based on a custom high-pressure (up to 34 MPa), high temperature (up to 250°C) variable-volume view cell (Thar Technologies),[68] was modified for observation of the foaming process. In this study, the volume of the cell was fixed to allow for a controlled pressure release rate. The pressure inside the cell was controlled by a syringe pump (ISCO 500D), which operated in a constant pressure mode. The temperature inside the cell was controlled by cartridge heaters and a temperature controller to an accuracy of ±0.5°C. A CCD camera with an adjustable lens was used to capture the video. The magnification was 180×. A Fiber-Lite model 181-1 gooseneck illumination system (Fisher Scientific) provided uniform back-lighting.

The sample was placed vertically in the sample holder and perpendicular to the view direction. The vessel was closed, and then pressurized with CO$_2$ to a desired pressure and temperature. The sample was allowed to equilibrate for 24 h. The pressure was then released quickly to atmospheric pressure. The entire process was monitored by the CCD camera. To avoid the effect of the metal sample holder on the sample, only the center part of the sample was in focus and recorded. The sample was then taken out for optical observation or SEM analysis. A scanning electron microscope (SEM, HITACHI S-4300) was used to observe the bubble morphology of foam samples.

As mentioned above, the thin-sheet sample was placed vertically in the sample holder and was perpendicular to the view direction. The "free-standing" sample did not touch any solid surface thus reducing the possibility of heterogeneous nucleation.

The effects of initial CO$_2$ pressure and temperature on the foaming process were investigated. Six foaming conditions, shown in Table I, were studied. Initial pressure and temperature, average pressure drop rate and maximum pressure drop rate are given. The final CO$_2$ pressure was atmospheric for all cases. These pressure and temperature combinations were chosen to make sure that the sample does not warp after 24 h of CO$_2$ saturation, foaming is uniform, and bubble number is small enough for counting. In addition, cases (1), (2), and (5) were used to study the temperature effect; cases (1), (3), and (4) were used to probe the pressure effect. Table I also features the three literature trials that we analyzed.

The maximum pressure drop rate in all cases we studied was less than 6 MPa/s. In contrast, the

TABLE I
Initial Conditions and Pressure Drop Rates for the Six Cases Studied (In All Cases, the Final Pressure was Atmospheric) and the Three Cases from the Literature to Obtain Quantitative Bubble Nucleation Rates in the PS-CO$_2$ System

Cases	Initial conditions	Solubility (wt % CO$_2$)	Average pressure drop rate (MPa/s)	Maximum pressure drop rate (MPa/s)
(1)	8.28 MPa, 80°C	6.12	1.00	4.66
(2)	8.28 MPa, 60°C	8.06	0.92	4.32
(3)	6.90 MPa, 80°C	5.17	0.94	4.46
(4)	10.34 MPa, 80°C	7.44	1.17	5.53
(5)	8.28 MPa, 70°C	6.99	0.91	4.06
(6)	10.34 MPa, 60°C	9.66	1.00	5.85
(L1)	21.07 MPa, 180°C	9.30	N/A	20
(L2)	14.83 MPa, 180°C	6.50	N/A	50
(L3)	10.00 MPa, 180°C	4.37	N/A	50

pressure drop rates reported in the literature[52] are from 6 to 220 MPa/s. Of these, we were able to analyze data only when the pressure drop rate was 20 MPa/s or higher. These higher pressure drop rates lead to much higher nucleation rates, which increase the likelihood that the bubbles will coalesce, making it difficult to get an accurate bubble count. Our use of smaller pressure drop rates may explain why we observed the bubbles much longer after the pressure drop (longer than 50 s in our cases and less than 1 s in the literature).

The whole foaming process was recorded and the movie was analyzed to obtain the bubble number density growth curve (bubble number density vs. time) whenever possible. Some issues with the clarity of the video rendered such analysis impossible in cases (2) and (4). Specifically, case (2) likely suffered from sample roughness or transparency issues that made identification of bubbles impossible and case (4) experienced dry ice formation due to the experimental conditions chosen, which completely blackened the images. These two cases have therefore been removed from the scaling curve analysis. After each foaming experiment was finished, images of the sample were taken by an optical microscope. In the microscopic images, we found that there was more than one layer of bubbles. A thin sample with thickness of 0.6 mm was used, and

yet the sample was still not thin enough to guarantee a single layer of bubbles because the bubble diameter was still much smaller than the thickness of the sample. When taking the images by a microscope, different depths in the sample were put into focus to obtain a series of images. These images were carefully compared to count the total bubble number. The final bubble density (optical) was calculated based on the total bubble number and sample dimension.

Figure 1 shows some representative snapshots from the movie for case (1). Where possible, we carefully compared the snapshots taken at every second to count the bubble numbers and obtained the curves of bubble number density versus time. These plots are shown in Figure 2 for each of the four cases that were analyzed. For case (1), we observe bubbles starting at around 60 s (where the bubble number density curve begins) and the other cases show similar behavior. Though nucleation occurred at an earlier, unknown time, we expect that relatively few bubbles nucleated before the pressure drop ended, allowing us to make the simplifying assumption that nucleation and pressure drop are decoupled, since the pressure drop finished within about 20 s, as can be seen in Figure 3. Similar pressure drop profiles were provided to us by Park's group for three of their trials. Specifically, these are
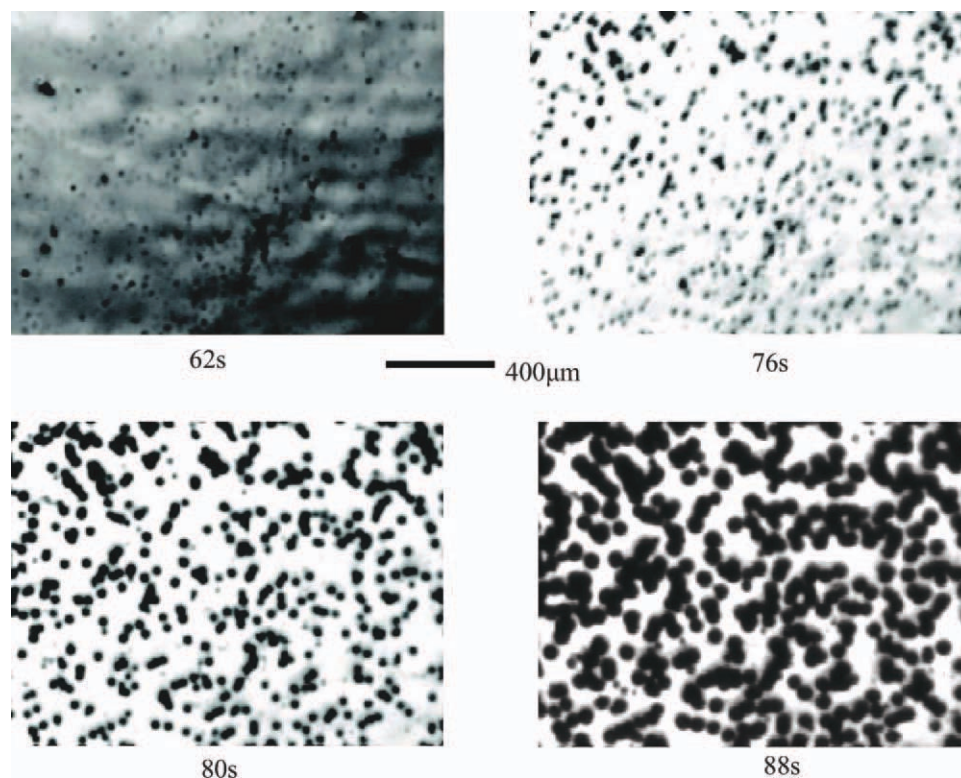

Figure 1 Representative snapshots at 62, 76, 80, and 88 s after the start of pressure drop for the PS foaming process with initial pressure 8.28 MPa and temperature 80°C [case (1)]. [Color figure can be viewed in the online issue, which is available at wileyonlinelibrary.com.]
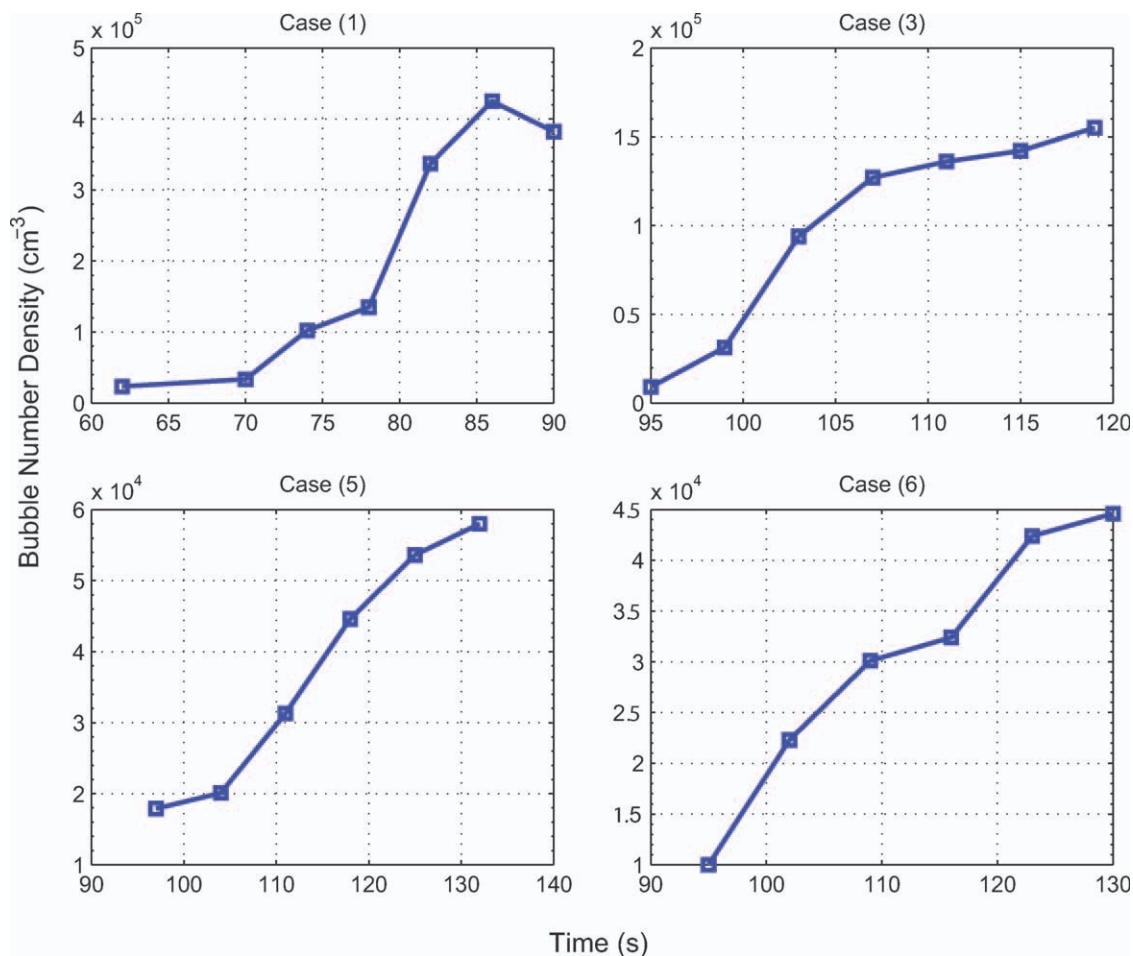
Figure 2 The bubble number density versus time curves for the PS foaming process for each case for which they could be constructed. [Color figure can be viewed in the online issue, which is available at wileyonlinelibrary.com.]

the trials with a maximum pressure drop rate of 20 MPa/s and the two with maximum pressure drop rates of 50 MPa/s. Since nucleation was observed before the pressure drop had concluded, the simplifying assumption used for our trials is not valid. It is therefore necessary to determine the pressure at select times from the pressure profiles and use those pressures, rather than the final pressure, when determining ΔP.

It should be noted that final bubble number densities determined by analyzing the movies and those from postexperiment optical microscope analysis can differ considerably. Table II summarizes the results based on the microscopic images and movies. In case (6), there were many layers of bubbles and these bubbles were close to each other; therefore, it was impossible to count the total number of bubbles. The optical bubble number density, 5.80×10^6 bubbles/cm^3, was calculated assuming the bubbles were uniformly distributed in all three dimensions. A lower number density from the movies relative to the optical value may be due to the presence of multiple layers of bubbles, which may not be visible in
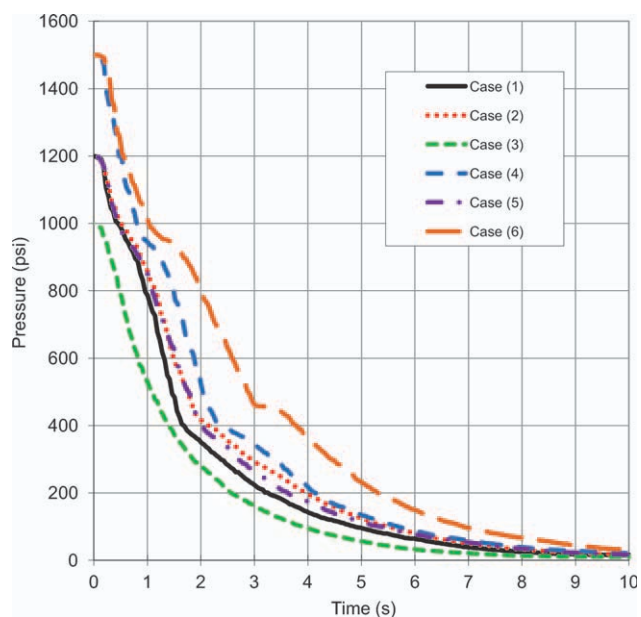

Figure 3 Pressure drop profiles during foaming for each of our cases. [Color figure can be viewed in the online issue, which is available at wileyonlinelibrary.com.]

TABLE II
Summary of the Initial and Final Conditions, Bubble Number Densities, and Foaming Start Times for all Cases

Case	Initial conditions	Final pressure[a] (MPa)	Final bubble number density (movies)[b] (cm^{-3})	Final bubble number density (optical) (cm^{-3})	Foaming start time[c] (s)
(1)	8.28 MPa, 80°C	0.10	4.25×10^5	1.05×10^5	70
(2)	8.28 MPa, 60°C	0.10	N/A	2.29×10^5	120
(3)	6.90 MPa, 80°C	0.10	1.55×10^5	7.98×10^4	95
(4)	10.34 MPa, 80°C	0.10	N/A	3.81×10^5	56
(5)	8.28 MPa, 70°C	0.10	5.80×10^4	1.52×10^5	97
(6)	10.34 MPa, 60°C	0.10	4.46×10^4	5.80×10^6	95
(L1)	21.07 MPa, 180°C	17.21	2.00×10^8	N/A	0.137
(L2)	14.83 MPa, 180°C	11.00	1.80×10^8	N/A	0.065
(L3)	10.00 MPa, 180°C	5.87	7.00×10^8	N/A	0.3

[a] For cases L1–L3, the final pressure is determined from number density curves and pressure profiles.
[b] Bubble number density versus time curves could not be constructed for cases 2 and 4.
[c] For cases 1–6, foaming start time is the time when the first bubbles are observed in the movie stills. For cases L1–L3, foaming start time is the time at which the bubble number density becomes non-zero.

the movies. A relatively higher number density from the movies compared to the optical observation may be due to bubble collapse/coalescence in the latter or the counting of artifacts in the movie stills that are not bubbles. Since the optical microscope images are clearer, these values are likely more accurate. However, since it is necessary to have dynamic data to obtain nucleation rates, the values from the movies are used for this purpose, as outlined below.

The bubble nucleation rate, defined as the number of nuclei formed per unit volume per unit time, can be obtained by differentiating the curve of bubble number density versus time with the assumption that one nucleus grows to one detectable bubble. Figures 6(b) and 7(b) in the literature[52] show the plots of bubble number density versus time under different initial pressures and pressure drop rates. Since the bubble number density has a rough linear relationship with time on the semi-log plots, a non-constant nucleation rate is obtained. This is expected because the supersaturation varies during the course of the pressure drop. This nonconstant nucleation rate can also be seen in Figure 2. Here, the variable rate can be attributed to more complex transient nucleation behavior or, perhaps, a local change in CO_2 concentration due to the presence of other nearby bubbles, rather than a global change in pressure. As a rough approximation, the endpoints of the bubble number density versus time curve are used to calculate the slope of the curve. This slope is taken to be the nucleation rate for these trials.

Once the nucleation rate is known, and ΔP has been calculated for the experimental conditions, eq. (1) is only a function of γ. Therefore, the value of γ can be determined. Upon finding a suitable value for γ_∞, ϕ can be determined for an experiment. The EOS can then be used to find the value of ξ. With these two quantities determined for a variety of experiments, an experimental scaling curve may be constructed.

RESULTS AND DISCUSSION

To facilitate the comparison of theoretical and experimental results, we need to be able to accurately predict phase diagrams of real systems using an EOS. S–L EOS parameter values for pure components are readily available in the literature.[69] Upon fitting to experimental solubility data[69,70] at several temperatures, we are able to determine the values for the binary interaction parameter, k_{ij}, of this system. A linear fitting of the values with respect to temperature was used for interpolation purposes. As an example, at 100°C, $k_{ij} = -0.075$ and the resulting phase diagram is shown in Figure 4, where the solid
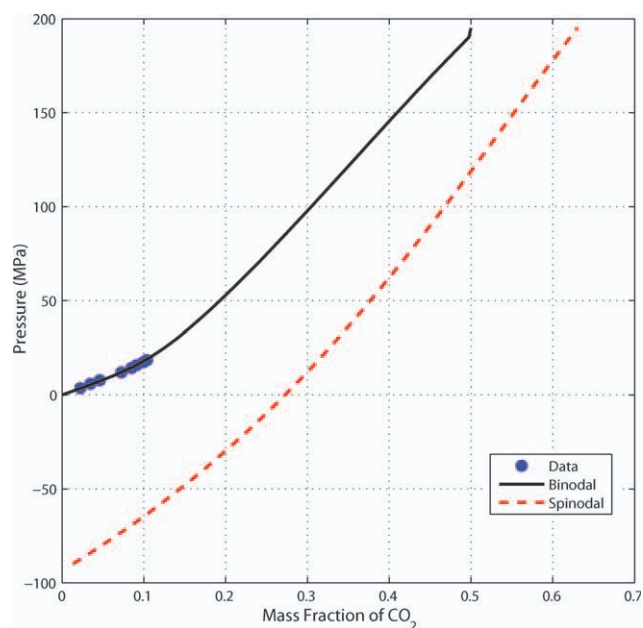

Figure 4 Binodal (solid curve) and spinodal (broken curve) curves of PS ($M_w = 187,000$)-CO_2 at 100°C by S–L EOS ($k_{ij} = -0.075$) (data points are from Sato et al.[69]). [Color figure can be viewed in the online issue, which is available at wileyonlinelibrary.com.]

TABLE III
Summary of Nucleation Rate Calculation Based on Bubble Number Density versus Time Curves for Available Cases

Case	Bubble number density (movies)[a] (cm^{-3})	Pressure drop time[b] (s)	Nucleation rate ($cm^{-3} s^{-1}$)
(1)	3.92×10^5	16	2.45×10^4
(3)	1.46×10^5	24	6.09×10^3
(5)	4.02×10^4	35	1.15×10^3
(6)	3.46×10^4	35	9.89×10^2
(L1)	2.00×10^8	0.188	1.06×10^9
(L2)	1.80×10^8	0.105	1.71×10^9
(L3)	7.00×10^8	0.5	1.40×10^7

[a] Bubble number densities for cases 1–6 are adjusted values. They are the difference between the final and initial bubble number density values on the bubble number density versus time curve.

[b] For cases 1–6, pressure drop time is the change in time from the first point to the last point on the bubble number density versus time curve. For cases L1–L3, the pressure drop time is the time at which the bubble number density curve ends. This discrepancy is due to the fact that in cases L1–L3, pressure drop and nucleation are not decoupled.

line is the binodal and the broken line is the spinodal. We are most interested in the region of pressure lower than 30 MPa, as this is the typical region for foaming processes.

To verify that the polymer could be modeled as a liquid, we checked that the glass transition temperature (T_g) of pure PS and the reduced T_g of the mixture (due to the presence of CO_2) were well below the temperatures used in the experiments.[71] The EOS can be used to determine the normalized degree of supersaturation, ξ, for each of the experiments. The nucleation rates determined from experiments are used to find the corresponding values for ϕ.

The bubble number densities (from bubble number density versus time curves) reported in Table II can be used to determine the nucleation rate for each case, using the methods described previously. These calculations are summarized in Table III. With known nucleation rate and ΔP, the value of γ can be found. However, to determine ϕ, it is necessary to find the value of γ_∞.

The data on the PS-CO_2 system are still very limited. Two sources are available, which provide data over a range of pressures for temperatures ranging from 200 to 230°C and for temperatures ranging from 170 to 210°C, respectively.[68,72] Both use the pendant drop method, which requires the calculation of the mixture density to find the surface tension. Comparing results at common values (200°C, PS685D), one finds that the two sources differ by as much as 2–3 dyne/cm, resulting in up to 15% relative error. The two primary reasons for these discrepancies are likely the use of different parameter

values to calculate the density and the inherent experimental error of this method. Indeed, data at other conditions by different researchers or different techniques do not match well either.[73] For the literature nucleation experiments, we chose to extrapolate the data by Li et al.[68] assuming that the interfacial tension between PS and CO_2 does not change very much with temperature at the elevated final pressures for these trials, as alluded to in the reference. These data were used because the same type of PS (Nova) was used in both Li's article and Ref. 52. No data for PS-CO_2 exists at lower temperatures and extrapolation of the required magnitude is not desirable. Since our trials end at atmospheric pressure and since CO_2 is not likely to interact greatly with PS at low pressure, we have chosen to use data for pure PS in an argon environment at atmospheric pressure to find γ_∞ for our experiments.[74] A small temperature extrapolation is still necessary. Once the values for γ_∞ are known for each of the experiments, it is possible to determine ϕ using eq. (6).

There are a few useful choices for determining the normalized degree of supersaturation since the thermodynamics are independent of path. These can most easily be compared on a P–x diagram (Fig. 5). The experimental method described here follows a vertical pathway to reach the final condition of the metastable melt phase. That is, the pressure is dropped while holding temperature and mass fraction of CO_2 constant. Approaching the final condition from a horizontal pathway is an equally valid approach. While it is difficult to conceive of an experimental setup to achieve this horizontal pathway, it is quite straightforward to do so from a theoretical perspective. A comparison of these methods is shown in
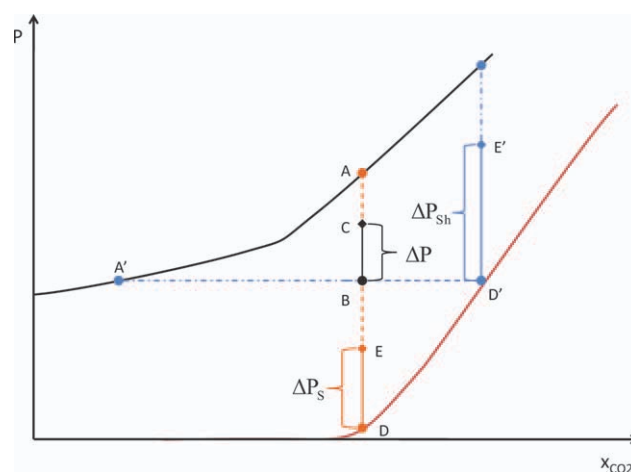

Figure 5 A schematic showing the vertical (dash) and horizontal (dash dot) methods of calculating the supersaturation, $\xi = \Delta P / \Delta P_s$. ΔP is the same in each case. The upper solid curve is the binodal and the lower solid curve is the spinodal. [Color figure can be viewed in the online issue, which is available at wileyonlinelibrary.com.]
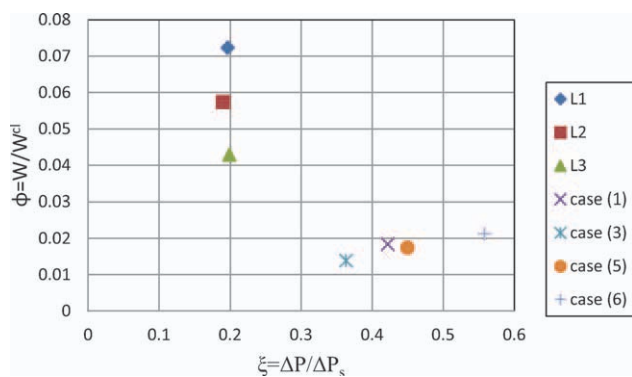
Figure 6 Relationship between W/W^{cl} and $\Delta P/\Delta P_s$, including three data points based on Guo's results[52] (first three points) and calculation based on our experimental results [cases (1), (3), (5), and (6)]. [Color figure can be viewed in the online issue, which is available at wileyonlinelibrary.com.]

Figure 5. The upper and lower solid lines demonstrate an example binodal and spinodal, respectively. The vertical approach is indicated by the dashed lines, while the horizontal pathway is marked by the dash dot lines. ΔP is the same in both cases.

The vertical approach begins at the binodal for a certain mass fraction of CO_2. This is point A. The final pressure (P^α), determined as described in the

Experimental Methods section, is marked by point B. The pressure at point C is the pressure of the hypothetical vapor phase having the same chemical potential of CO_2 as that of CO_2 in the metastable melt phase. This pressure corresponds to P^β and, together with P^α, defines ΔP. It should be noted that the location of point C is merely intended to show the magnitude of ΔP and not to imply that the hypothetical vapor phase has a mass fraction of CO_2 equal to that of CO_2 in the metastable melt. Indeed, the hypothetical vapor phase is pure CO_2. Point D indicates the spinodal point corresponding to the experimental pressure drop, which has the same mass fraction as points A and B. Similar to point C, point E indicates the pressure of the hypothetical vapor phase for the calculation of ΔP at the spinodal. It is merely intended to show the magnitude of ΔP_s. In the low CO_2 mass fraction region, point D (and sometimes point E) is found to have a negative pressure. While this is, from a theoretical standpoint, not a significant issue, it is, nonetheless, a bit awkward to consider conceptually.

The horizontal pathway, on the other hand, begins from the binodal point indicated by point A'. This point has the same pressure as the final point (still point B), but a different mass fraction. Since the final point is still located at B, the
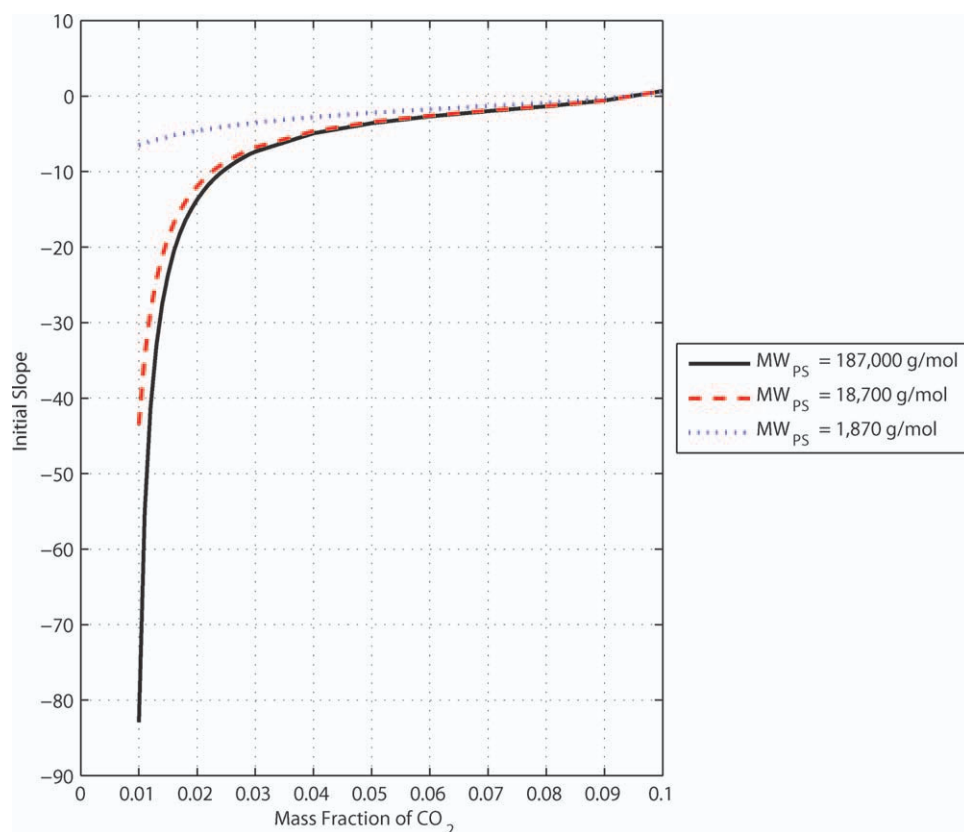

Figure 7 Summary of the initial slope calculation with different mass fractions of CO_2 and also polymers with different molecular weights. [Color figure can be viewed in the online issue, which is available at wileyonlinelibrary.com.]

definition of ΔP does not change, so P^{β} is still the pressure at C. However, the spinodal point that corresponds to this approach is indicated by point D'. This point is located horizontally from A' and B, so that it is at the same pressure, but at a different mass fraction. Determination of ΔP at this spinodal point locates the pressure of the hypothetical vapor phase which corresponds to the pressure at point E'. The difference between this pressure and that of the point D' (which is still P^{α}) defines ΔP_{sh}. This value is different from the one computed from the vertical pathway.

The value of ξ will change depending on which pathway is followed and the corresponding scaling curve will also change. However, the scaling approach is still valid in either case, but the initial slope used in the scaling function will change to accommodate the data. The horizontal pathway is utilized for calculations in this study, as it avoids the use of negative pressures and makes the trend of the experimental results easier to see.

Upon calculation of the normalized degree of supersaturation, ξ, an experimental scaling curve may be constructed. This curve is shown in Figure 6. In general, the four data points from our experiments are in a narrow interval of ξ because the magnitude of the pressure drops we used were still very large. Pressure drops that result in $\xi < 0.2$ are difficult to achieve experimentally, but clearly are desirable in evaluating the accuracy of the DIT prediction of the scaling function.

As can be seen, while the curve is monotonically decreasing, the concavity is inverted from what was observed in many scaling studies previously (such as Fig. 2 of Ref. 37). This indicates that the concavity, and hence the initial slope, depends on molecular weight. As Figure 7 demonstrates, the initial slope of the scaling curve, as determined from DIT, decreases with decreasing molecular weight. If the slope were less than 1, the concave down behavior demonstrated in Ref. 37 would be observed. Our result is consistent with the result shown by Muller et al.[75] (in Fig. 6), which shows a concave-up scaling curve for a hexadecane-CO$_2$ system.

Many of the quadratic functional forms seen previously[46,76] cannot represent a concave-up scaling curve. One quadratic form that directly includes the initial slope[45] can capture concave-up behavior, but not with the large negative slopes that we expect to see based on the experiments. We have thus chosen a functional form:

$$\frac{W}{W^{cl}} = \frac{1 - \xi}{1 - (1 + c)\xi} \quad (28)$$

where the parameter c corresponds to the initial slope determined from DIT. Using eq. (25) and fol-
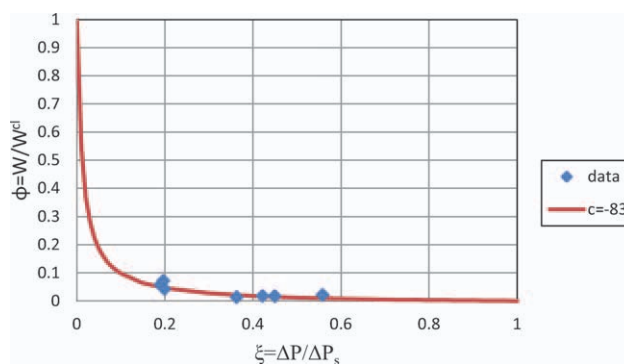

Figure 8 The experimental scaling data, with the scaling function based on DIT results ($c = -83$) superimposed. [Color figure can be viewed in the online issue, which is available at wileyonlinelibrary.com.]

lowing the calculation procedure described previously, the initial slope may be determined for the PS-CO$_2$ system. In order for this procedure to be valid, the final pressure must be sufficiently close to the initial pressure so that the slope found is that near saturation. However, if the pressure drop, and thus ΔP, is too small, numerical issues in the calculation may arise. To that end, we have chosen to set the value of the final pressure at 90% of the binodal pressure for a given mass fraction of CO$_2$. We set the temperature at 60°C and calculated the initial slope for a series of mass fractions. This is how Figure 7 was constructed.

The results for the PS with the molecular weight from experiment are indicated by the solid black line. Since no particular condition is more valid than another, we have chosen the value that most closely agrees with the experimental results. This indicates an initial slope of $c = -83$, which corresponds to a mass fraction of 0.01. This slope is much greater than what is observed in the literature.[75] The much higher molecular weight of our PS over the hexadecane used in that study likely explains the difference. Figure 8 shows the experimental results with the scaling function superimposed.

As we discussed earlier, the initial slope predicted by DIT depends upon the molecular weight of the polymer. Experimental examination of other polymer–gas systems could provide more insight into the effect of molecular weight on the DIT prediction, as well as further exploring the applicability and robustness of the scaling function that we have used.

CONCLUSIONS

Nucleation is a very complex phenomenon in physical foam processing and experimental and theoretical studies cannot provide all of the information necessary for a clear picture. The scaling approach described

here provides a way to access experimentally inaccessible quantities (such as the reversible work to form a critical nucleus, W) using phase diagrams. By using DIT to determine the initial slope of the scaling curve, one can determine the scaling function accurately if a suitable one-parameter equation, such as eq. (28), is assumed without resorting to curve fitting.

The novel free-standing sample setup mitigated heterogeneous nucleation and provided quantitative data for homogenous nucleation rate.

The use of the Sanchez–Lacombe EOS worked very well for bulk phase diagram calculations, but presented difficulties when entropy calculations were required for DIT. The use of a more accurate equation of state would likely make the results more quantitatively accurate. Nonetheless, the current predicted scaling function agrees with current experimental results and qualitatively agrees with the findings of other researchers. The power of this scaling approach is evident in the fact that, in principle, it is possible to predict nucleation behavior using only bulk thermodynamic quantities, which are experimentally accessible. While the examination of additional systems and further verification of results are needed, this scaling approach shows great promise.

APPENDIX A: INTERMEDIATE STEPS IN DIT DERIVATION

Derivation of eq. (10)

Rearranging eq. (9),

$$u_N^l - Ts_N^l + \frac{P^l}{\rho^l} = \sum_i \mu_i x_i^l \qquad (A1)$$

Subtracting eq. (9) from eq. (8):

$$\omega(\bar{r}) - \omega^l = \rho(\bar{r})\left[u_N(\bar{r}) - Ts_N(\bar{r}) - \sum_i \mu_i x_i(\bar{r})\right]$$
$$- \rho^l\left[u_N^l - Ts_N^l - \sum_i \mu_i x_i^l\right] \qquad (A2)$$

Using eqs. (A1) and (9):

$$\omega(\bar{r}) - \omega^l = \rho(\bar{r})\left[u_N(\bar{r}) - Ts_N(\bar{r}) - \sum_i \mu_i x_i(\bar{r})\right.$$
$$\left. + \sum_i \mu_i x_i^l - \sum_i \mu_i x_i^l\right] + P^l$$

$$= \rho(\bar{r})\left\{u_N(\bar{r}) - Ts_N(\bar{r})\right.$$
$$\left. - \sum_i \mu_i\left[x_i(\bar{r}) - x_i^l\right] - u_N^l + Ts_N^l - \frac{P^l}{\rho^l}\right\} + P^l$$
$$= \rho(\bar{r})\left[\Delta u_N(\bar{r}) - \Delta Ts_N(\bar{r}) - \sum_i \mu_i \Delta x_i(\bar{r})\right]$$
$$+ P^l\left(1 - \frac{\rho(\bar{r})}{\rho^l}\right)$$
$$= \rho(\bar{r})\left[\Delta u_N(\bar{r}) - \Delta Ts_N(\bar{r})\right.$$
$$\left. - \sum_i \mu_i \Delta x_i(\bar{r}) + P^l \Delta v(\bar{r})\right]$$
$$\omega(\bar{r}) - \omega^l = \Delta\chi(\bar{r}) - T\Delta s(\bar{r})r \qquad (A3)$$

where $\Delta A_N(\bar{r}) := A_N(\bar{r}) - A_N^l$ for $A = u, s$

$$\Delta x_i(\bar{r}) := x_i(\bar{r}) - x_i^l$$
$$\Delta v(\bar{r}) := \left(\frac{1}{\rho(\bar{r})} - \frac{1}{\rho^l}\right)$$
$$\Delta\chi(\bar{r}) := \rho(\bar{r})\left\{u_N(\bar{r}) - u_N^l - \sum_i \mu_i\left[x_i(\bar{r}) - x_i^l\right]\right.$$
$$\left. + P^l\left[\frac{1}{\rho(\bar{r})} - \frac{1}{\rho^l}\right]\right\} \qquad (A4)$$
$$\Delta s(\bar{r}) := \rho(\bar{r})\left[s_N(\bar{r}) - s_N^l\right] \qquad (A5)$$

Derivation of eq. (13)

Applying eq. (A4) to a homogeneous vapor phase with the same temperature and chemical potential as the liquid phase:

$$\Delta\chi^v = \rho^v\left\{u_N^v - u_N^l - \sum_i \mu_i\left[x_i^v - x_i^l\right] + P^l\left[\frac{1}{\rho^v} - \frac{1}{\rho^l}\right]\right\} \qquad (A6)$$

$$\Delta\chi^v = \rho^v\left\{u_N^v - u_N^l - \sum_i \mu_i x_i^v + \sum_i \mu_i x_i^l + P^l v^v\right.$$
$$\left. - P^l v^l + P^v v^v - P^v v^v\right\}$$
$$= \rho^v\left\{u_N^v + P^v v^v - \sum_i \mu_i x_i^v - (P^v - P^l)v^v\right.$$
$$\left. - u_N^l - P^l v^l - \sum_i \mu_i x_i^l\right\}$$

Applying eq. (A1) to the last three terms and the first three terms (substituting v for l):

$$\Delta\chi^v = \rho^v\left[Ts_N^v - (P^v - P^l)v^v - Ts_N^l\right] \quad (A7)$$

from which we obtain eq. (13), where:

$$\Delta s_N^v := s_N^v - s_N^l \quad (A8)$$

Derivation of eq. (15)

Beginning from eq. (14):

$$W = 4\pi\int_0^{+\infty}\left[\omega\left(\bar{r}\right) - \omega^v - (\omega^l - \omega^v)\right]r^2 dr \quad (A9)$$

Substituting in eq. (13), we obtain:

$$W = 4\pi\int_0^{+\infty}\left[\omega\left(\bar{r}\right) - \omega^v + \Delta P^l\right]r^2 dr \quad (A10)$$

Now apply eq. (A3):

$$W = 4\pi\int_0^{+\infty}\left[\Delta\chi\left(\bar{r}\right) - T\Delta s\left(\bar{r}\right) + \Delta P^l\right]r^2 dr \quad (A11)$$

$$W = \frac{4\pi}{3}\lim_{R\to\infty}\left[\Delta\chi^l\left(R^3 - R_\chi^3\right) - T\Delta s^l\left(R^3 - R_s^3\right) + \Delta P^l R^3\right] \quad (A12)$$

Rearranging eq. (13), it can be shown that $\Delta\chi^l - T\Delta s^l + \Delta P^l = 0$ and thus:

$$W = -\frac{4\pi}{3}\left[\Delta\chi^l R_\chi^3 - T\Delta s^l R_s^3\right] \quad (A13)$$

Now, let $\delta_G = R_s - R_\chi$ and substitute in for R_χ to obtain eq. (15).

Derivation of eq. (16)

Assuming that R_s does not depend on δ_G, maximize eq. (15) with respect to R_s:

$$\frac{\partial W}{\partial R_s} = -4\pi\left[\Delta\chi^l(R_s - \delta_G)^2 - T\Delta s^l R_s^2\right]$$
$$= -4\pi\left[\Delta\chi^l R_s^2 - 2\Delta\chi^l R_s\delta_G + \Delta\chi^l\delta_G^2 - T\Delta s^l R_s^2\right]$$

Applying eq. (13) to the first and last terms:

$$\frac{\partial W}{\partial R_s} = -4\pi\left[-\Delta P^l R_s^2 - 2\Delta\chi^l R_s\delta_G + \Delta\chi^l\delta_G^2\right]$$
$$= 4\pi\Delta P^l\left[R_s^2 + 2\frac{\Delta\chi^l}{\Delta P^l}R_s\delta_G - \frac{\Delta\chi^l}{\Delta P^l}\delta_G^2\right] \quad (A14)$$

Letting

$$\zeta := -\frac{\Delta\chi^l}{\Delta P^l} = 1 - \frac{T\Delta s^l}{\Delta P^l}, \quad (A15)$$

$$\frac{\partial W}{\partial R_s} = 4\pi\Delta P^l\left[R_s^2 + 2\zeta R_s\delta_G - \zeta\delta_G^2\right]$$
$$= 4\pi\Delta P^l\left[R_s^2 + 2\zeta R_s\delta_G - \zeta\delta_G^2 - \zeta^2\delta_G^2 + \zeta^2\delta_G^2\right]$$
$$\frac{\partial W}{\partial R_s} = 4\pi\Delta P\left[(R_s - \delta_G\zeta)^2 + \delta_G^2\zeta(1 - \zeta)\right] \quad (A16)$$

Case 1: $\Delta\chi^l < 0$

Since $\Delta P^l < 0$ for bubble nucleation,

$$\zeta = -\frac{\Delta\chi^l}{\Delta P^l} < 0.$$

So, from eq. (A16), the local maximum of W, denoted as W^*, is:

$$R_s^* = \delta_G\zeta + \sqrt{\delta_G^2\zeta(\zeta - 1)}$$
$$= \delta_G\zeta + |\delta_G\zeta|\sqrt{1 - \frac{1}{\zeta}} \quad (A17)$$

Since $\zeta < 0$, this becomes:

$$R_s^* = \delta_G\zeta - \zeta|\delta_G|q = \zeta(\delta_G - |\delta_G|q), \quad (A18)$$

where

$$q := \sqrt{1 - \frac{1}{\zeta}} > 1 \quad (A19)$$

Since $q > 1$, the condition that $R_s^* > 0$ does not determine the sign of δ_G. If we let $\delta_G > 0$, then eq. (A18) becomes:

$$R_s^* = \zeta(\delta_G - \delta_G q)$$
$$= \zeta\delta_G(1 - q) > 0 \quad (A20)$$

If we instead let $\delta_G < 0$, we obtain:

$$R_s^* = \zeta\delta_G(1 + q) > 0. \quad (A21)$$

Either way, $R_s^* > 0$, as required. However, we know that $\delta_{G0} > 0$ for the flat interface and that $\delta_G > 0$ for liquid droplets.[44,45] This means that the dividing surface associated with $\Delta\chi$ penetrates the liquid deeper than the dividing surface associated with Δs. We expect that the same will hold true for sufficiently large bubbles. Since the liquid and vapor phases have been reversed (i.e., bubble instead of liquid droplet), this means that $R_\chi > R_s > 0$, so in the low supersaturation limit:

$$\delta_G = R_s - R_\chi < 0. \quad (A22)$$

If we assume that δ_G changes continuously with supersaturation, then $\delta_G > 0$ would be mathematically possible provided that $\delta_G = 0$ at some supersaturation. R_s^* would then be zero and thus W^* would be zero at that supersaturation also. However, that can only be true at the spinodal, which invalidates the possibility of having non-zero W^* for $\delta_G > 0$. Thus, we demand that eq. (A22) hold for all bubbles. It should be noted that this argument depends upon the assumption that δ_G is independent of R_s, which is to say that it only applies to sufficiently large bubbles. Once eq. (A22) is established, it can be applied to eq. (15) to continue the derivation of DIT for a binary system undergoing bubble nucleation.

Case 2: $\Delta\chi^l > 0$

Since $\Delta P^l < 0$ for bubble nucleation,

$$\zeta = -\frac{\Delta\chi^l}{\Delta P^l} > 0.$$

So, from eq. (A16), the local maximum of W, denoted as W^*, is:

$$R_s^* = \delta_G\zeta + \sqrt{\delta_G^2\zeta(\zeta-1)}$$
$$= \delta_G\zeta + |\delta_G\zeta|\sqrt{1 - 1/\zeta} \tag{A23}$$

Since $\zeta > 0$, this becomes:

$$R_s^* = \delta_G\zeta + |\delta_G|\zeta\sqrt{1 - 1/\zeta} = \zeta(\delta_G + |\delta_G|q), \tag{A24}$$

where

$$q := \sqrt{1 - 1/\zeta} < 1 \tag{A25}$$

Since $q < 1$, we expect that $\delta_G > 0$ should hold. In that case,

$$R_s^* = \zeta(\delta_G + \delta_G q)$$
$$= \zeta\delta_G(1+q) > 0, \tag{A26}$$

as we expect. For the sake of completeness, if we let $\delta_G < 0$, we get:

$$R_s^* = \zeta(\delta_G - \delta_G q)$$
$$= \zeta\delta_G(1-q) < 0. \tag{A27}$$

This possibility fails the requirement that $R_s^* > 0$, as expected. So for this case, we demand that $\delta_G > 0$. However, as case 1 demonstrated, $\delta_G < 0$ must hold for sufficiently large bubbles and allowing both

conditions requires an unphysical transition where $\delta_G = 0$ (and thus $W^* = 0$) at a supersaturation other than the spinodal. Therefore, the DIT framework breaks down if $\Delta\chi^l > 0$ for bubble nucleation and case 1 must be followed for further derivation to be possible.

Derivation of eq. (21)

$$W^* = \frac{4\pi}{3}\left\{\Delta\chi^l[\delta_G\zeta(1+q) - \delta_G]^3 - T\Delta s^l[\delta_G\zeta(1+q)]^3\right\}$$
$$= \frac{4\pi}{3}\delta_G^3\left\{\Delta\chi^l[\zeta(1+q) - 1]^3 - T\Delta s^l[\zeta(1+q)]^3\right\} \tag{A28}$$

Dividing through by $-\Delta P^l$ and applying eq. (A17):

$$W^* = -\frac{4\pi}{3}\delta_G^3\Delta P^l\left\{\zeta[\zeta(1+q) - 1]^3 + (1-\zeta)[\zeta(1+q)]^3\right\} \tag{A29}$$

Now consider the term in the curly brackets:

$$\{\ldots\} = \zeta[\zeta(1+q) - 1][\zeta(1+q) - 1][\zeta(1+q) - 1]$$
$$+ (1-\zeta)[\zeta(1+q)]^3$$
$$= \zeta\Big[[\zeta(1+q)]^3 - 3[\zeta(1+q)]^2 + 3[\zeta(1+q)] - 1\Big]$$
$$+ [\zeta(1+q)]^3 - \zeta[\zeta(1+q)]^3$$
$$= -3\zeta[\zeta(1+q)]^2 + 3\zeta[\zeta(1+q)] - \zeta + [\zeta(1+q)]^3$$
$$= \zeta^3(1+q)^2[(1+q) - 3] + 3\zeta^2(1+q) - \zeta$$
$$= \zeta^3(1+q)^2(q-2) + 3\zeta^2(1+q) - \zeta$$
$$= \zeta^3(1 + 2q + q^2)(q-2) + 3\zeta^2(1+q) - \zeta$$
$$= \zeta^3\left(1 + 2q + 1 - 1/\zeta\right)(q-2) + 3\zeta^2(1+q) - \zeta$$
$$= 2\zeta^3(1+q)(q-2) - \zeta^2(q-2) + 3\zeta^2(1+q) - \zeta$$
$$= 2\zeta^3(q - 2 + q^2 - 2q) + \zeta^2[3(1+q) - (q-2)] - \zeta$$
$$= 2\zeta^3\left(1 - 1/\zeta - q - 2\right) + \zeta^2[3(1+q) - (q-2)] - \zeta$$
$$= -2\zeta^3(1+q) - 2\zeta^2 + \zeta^2(2q+5) - \zeta$$
$$= -2\zeta^3(1+q) + \zeta^2(2q+3) - \zeta$$
$$= -\zeta[2\zeta2(1+q) - \zeta(2q+3) + 1]$$
$$\{\ldots\} = -\zeta[2(1+q)\zeta - 1](\zeta - 1)$$

Substituting back into eq.(A29):

$$W^* = -\frac{4\pi}{3}\delta_G^3\Delta P^l\{-\zeta[2(1+q)\zeta - 1](\zeta - 1)\} \tag{A30}$$

$$W^* = -\frac{4\pi}{3}\delta_G^3\Delta P^l\psi_G \tag{A31}$$

where

$$\psi_G := \zeta(\zeta - 1)[2(1+q)\zeta - 1] \tag{A32}$$

APPENDIX B: DERIVATION OF INITIAL SLOPE EQUATION FROM DIT

Recall eq. (24):

$$\phi = \frac{1}{4}\left(\frac{\Delta P^l}{L_0}\right)^3 \psi_G \qquad (B1)$$

where

$$\psi_G = \zeta(\zeta-1)[2(1+q)\zeta - 1] \text{ and } q = \sqrt{1 - \tfrac{1}{\zeta}} \quad (B2)$$

Let $x = \Delta P^l = P^l - P^v < 0$ and $y = -T\Delta s^l > 0$.
So now

$$\zeta = 1 + \frac{y}{x} < 0 \text{ and } x\zeta = x + y > 0 \qquad (B3)$$

Further,

$$\zeta q = \zeta\sqrt{1 - \tfrac{1}{\zeta}} = -|\zeta|\sqrt{1 - \tfrac{1}{\zeta}} = -\sqrt{\zeta^2\left(1 - \tfrac{1}{\zeta}\right)}$$

$$= -\sqrt{\zeta(\zeta-1)} = -\sqrt{\left(1+\frac{y}{x}\right)\left(\frac{y}{x}\right)} \qquad (B4)$$

The portion of eq. (B1) that is a function of x is merely $\Delta P^l \psi_G$. Replacing ψ_G with eq. (B2) and substituting in eqs. (B3) and (B4):

$$(\Delta P^l)^3 \psi_G = x^3 \psi_G = x^3\left\{\left(1+\frac{y}{x}\right)\left(\frac{y}{x}\right)\left[2\left(1+\frac{y}{x}\right)\right.\right.$$

$$\left.\left. - 2\sqrt{\left(1+\frac{y}{x}\right)\left(\frac{y}{x}\right)} - 1\right]\right\}$$

$$x^3\psi_G = (x+y)y\left[2(x+y) + 2\sqrt{(x+y)y} - x\right]$$

$$(B5)$$

Continuing to manipulate eq. (B5), it can be shown that:

$$x^3\psi_G = (x+y)^2 y + (x+y)y^2 + 2[(x+y)y]^{\frac{3}{2}}. \quad (B6)$$

Now take the derivative of eq. (B6) with respect to x (noting that y is a function of x):

$$\left(\frac{\partial(x^3\psi_G)}{\partial x}\right)_{x=0} = 2(1+y')y^2 + y'y^2 + (1+y')y^2$$

$$+ 2y'y^2 + 3y[(1+y')y + y'y]$$

$$= 6y^2(1+2y')$$

Switching variables back from x and y:

$$\left(\frac{\partial\left[(\Delta P^l)^3\psi_G\right]}{\partial\Delta P}\right)_{\Delta P^l=0} = 6(-T\Delta s_0^l)^2\left[1 + 2\frac{\partial(-T\Delta s^l)}{\partial\Delta P^l}\right]$$

$$(B7)$$

Since $-T\Delta s_0^l = L_0$ (see Ref. 45),

$$\left(\frac{\partial\left[(\Delta P^l)^3\psi_G\right]}{\partial\Delta P^l}\right)_{\Delta P^l=0} = 6(L_0)^2\left[1 - 2\frac{\partial(T\Delta s^l)}{\partial\Delta P^l}\right]$$

Therefore, the derivative of eq. (B1) is:

$$\frac{\partial\phi}{\partial\Delta P^l} = \frac{1}{4(L_0)^3}\frac{\partial\left[(\Delta P^l)^3\psi_G\right]}{\partial\Delta P^l} = \frac{3}{2L_0}\left[1 - 2\frac{\partial(T\Delta s^l)}{\partial\Delta P^l}\right].$$

$$(B8)$$

Since $\xi = \Delta P / \Delta P_s = \Delta P^l / \Delta P_s^l$

$$\therefore \left(\frac{\partial\phi}{\partial\xi}\right)_{\xi=0} = \frac{3\Delta P_s^l}{2L_0}\left[1 - 2\frac{\partial(T\Delta s^l)}{\partial\Delta P^l}\right]. \qquad (B9)$$

References

1. Klempner, D.; Sendijarevic, V. Handbook of Polymer Foams and Foam Technology; Hanser Gardener Publications: Cincinnati, 2004, pp 1–4, 214–220.
2. Arora, A.; Padua, G. J Food Sci 2010, 75, R43.
3. Wake, C. M.; Gupta P. K.; Mikos, G. A. Cell Transpl 1996, 5, 465.
4. Martinez-Perez, C. A.; Garcia-Casillas, P. E.; Romero, P.; Juarez, C.; Martinez-Villafane, C. A.; Moller, A. D.; Romero-Garcia, J. J Adv Mater, 2006, 5.
5. US Census Bureau. 2007 Economic Census; Sector 31: Manufacturing Industry Series, 2007.
6. UNEP, The Montreal Protocol on Substances that Deplete the Ozone Layer, Nairobi, Kenya, 2000.
7. Arora, A. K.; Lesser, A. J.; McCarthy, J. T. Macromolecules 1998, 31, 4614.
8. Park C. B.; Suh, P. N. Polym Eng Sci 1996, 36, 34.
9. Park, C. B.; Suh, N. P.; Baldwin, D. F. U.S. Pat. 5,866,053 (1999).
10. Han, X. Continuous Production of Microcellular Foams, PhD Dissertation, The Ohio State University, 2003; p 356.
11. Han, X.; Koelling, W. K.; Tomasko, D.; Lee, J. L. In 58th Annual Technical Conference—Society of Plastics Engineers, 2000; pp 1857–1861.
12. Han, X.; Koelling, W. K.; Tomasko, D. L.; Lee, J. L. Polym Eng Sci 2002, 42, 2094.
13. Lee, J. L.; Zeng, C.; Cao, X.; Han, X.; Shen, J.; Xu, G. Compos Sci Technol 2005, 65, 2344.
14. Shen, J.; Zeng, C.; Lee, J. L. Polymer 2005, 46, 5218.
15. Shen, J. Application of nanoparticles in polymeric foams, PhD Dissertation, In Chemical Biomolecular Engineering Department, The Ohio State University: Columbus, OH, 2006; p 263.
16. Lee, C. P.; Wang, J.; Park, B. C. In 63rd Annual Technical Conference—Society of Plastics Engineers, 2005; pp 2660–2664.
17. Lee, C. P.; Wang, J.; Park, B. C. Ind Eng Chem Res 2006, 45, 175.
18. Park, B. C.; Padareva, V.; Lee, P. C.; Naguib, E. H. J Polym Eng 2005, 25, 239.
19. Taki, K.; Nitta, K.; Kihara, S.-I.; Ohshima, M. J Appl Polym Sci, 2005, 97, 1899.
20. Han, X.; Shen, J.; Wingert, M.; Lee, J. L. In 64th Annual Technical Conference—Society of Plastics Engineers, 2006; pp 2695–2699.
21. Pop-iliev, R.; Liu, F.; Liu, G.; Park, B. C. Adv Polym Technol 2003, 22, 280.
22. Kim, Y. K.; Kang, S. L.; Kwak, H.-Y. Polym Eng Sci 2004, 44, 1890.
23. Strey, R.; Wagner, P. E.; Viisanen, Y. J Phys Chem 1994, 98, 7748.

24. Colton, J. S.; Suh, P. N. Polym Eng Sci 1987, 27, 500.
25. Colton, J. S.; Suh, P. N. Polym Eng Sci 1987, 27, 485.
26. Colton, J. S.; Suh, P. N. Polym Eng Sci 1987, 27, 493.
27. Lee, J. G.; Flumerfelt, W. R. J Coll Interface Sci 1996, 184, 335.
28. Han, J. H.; Han, D. C. J Polym Sci, Part B: Polym Phys 1990, 28, 711.
29. Han, J. H.; Han, D. C. J Polym Sci, Part B: Polym Phys 1990, 28, 743.
30. Goel, S. K.; Beckman, J. E. Polym Eng Sci 1994, 34, 1137.
31. Goel, S. K.; Beckman, J. E. Polym Eng Sci 1994, 34, 1148.
32. Goel, S. K.; Beckman, J. E. AIChE J 1995, 41, 357.
33. Nishioka, K. Phys Script T 1992, T44, 23.
34. Schmelzer, J. W. P. Mater Phys Mech 2003, 6, 21.
35. Blander, M.; Katz, L. J. AIChE J 1975, 21, 833.
36. Gibbs, J. W. In The Scientific Papers of Willard Gibbs J. Volume One: Thermodynamics; Ox Bow, Woodbridge, CN, 1993; pp 252–254.
37. Kusaka, I. J Chem Phys 2003, 118, 5510.
38. Nishioka, K. Phys Rev A 1987, 36, 4845.
39. Talanquer, V. J Chem Phys 1997, 106, 9957.
40. Palmer, G.; Demarquette, N. R. Polymer 2003, 44, 3045.
41. Reiss, H.; Tabazadeh, A.; Talbot, J. J Chem Phys 1990, 92, 1266.
42. Talanquer, V.; Oxtoby, W. D. J Phys Chem 1995, 99, 2865.
43. Gránásy, L. Europhys Lett 1993, 24, 121.
44. Gránásy, L.; Pusztai, T.; Hartmann, E. J Cryst Growth 1996, 167, 756.
45. Kusaka, I. J Chem Phys 2003, 119, 1808.
46. McGraw, R.; Laaksonen, A. Phys Rev Lett 1996, 76, 2754.
47. Talanquer, V. J Chem Phys 1997, 106, 9957.
48. Iland, K.; Wedekind, J.; Woelk, J.; Wagner, P. E.; Strey, R. J Chem Phys 2004, 121, 12259.
49. Rathke, B.; Baumgartl, H.; Strey, R. AIP Conf Proc 2000, 534, 414.
50. Taki, K.; Nakayama, T.; Yatsuzuka, T.; Ohshima, M. J Cell Plast 2003, 39, 155.
51. Taki, K.; Yanagimoto, T.; Funami, E.; Okamoto, M.; Ohshima, M. Polym Eng Sci 2004, 44, 1004.
52. Guo, Q.; Wang, J.; Park, C. B.; Ohshima, M. Ind Eng Chem Res 2006, 45, 6153.
53. Liu, K.; Erdogan, K. J Supercrit Fluids 1999, 16, 59.
54. Sanchez, I. C. In Encyclopedia of Physical Science and Technology; Academic Press: Boston, 1987; pp 1–18.
55. Sanchez, I. C. L.; Robert, H. J Phys Chem 1976, 80, 2352.
56. Lacombe, R. H.; Sanchez, C. I. J Phys Chem 1976, 80, 2568.
57. Sanchez, I. C.; Lacombe, H. R. J Polym Sci: Polym Lett Ed 1977, 15, 71.
58. Sanchez, I. C.; Lacombe, H. R. Macromolecules 1978, 11, 1145.
59. Liu, D.; Li, H.; Noon, M. S.; Tomasko, D. Macromolecules 2005, 38, 4416.
60. Sato, Y.; Fujiwara, K.; Takikawa, T.; Sumarno; Takishima, S.; Masuoka, H. Fluid Phase Equilib 1999, 162, 261.
61. Sato, Y.; Yurugi, M.; Fujiwara, K.; Takishima, S.; Masuoka, H. Fluid Phase Equilib 1996, 125, 129.
62. Kiran, E.; Xiong, Y.; Zhuang, W. J Supercrit Fluids 1993, 6, 193.
63. Xiong, Y.; Erdogan, K. Polymer 1994, 35, 4408.
64. Gibbs, J. W. In The Scientific Papers of Willard Gibbs J. Volume One: Thermodynamics; Ox Bow, Woodbridge, CN, 1993; pp 219–229.
65. Gránásy, L. J Non-Cryst Solids 1993, 162, 301.
66. Condo, D. P.; Sanchez, C. I.; Panayiotou, C. G.; Johnston, P. K. Macromolecules 1992, 25, 6119.
67. Panayiotou, C.; Vera, J. J Polym Sci, Part C: Polym Lett 1984, 22, 601.
68. Li, H.; Lee, L. J.; Tomasko, L. D. Ind Eng Chem Res 2004, 43, 509.
69. Sato, Y.; Takikawa, T.; Takishima, S.; Masuoka, H. J Supercrit Fluids 2001, 19, 187.
70. Hilic, S.; Boyer, S. A. E.; Padua, A. A. H.; Grolier, J.-P. E. J Polym Sci, Part B: Polym Phys 2001, 39, 2063.
71. Tomasko, L. D.; Li, H.; Liu, D.; Han, X.; Wingert, J. M.; Lee, L. J.; Koelling, W. K. Ind Eng Chem Res 2003, 42, 6431.
72. Park, H.; Thompson, B. R.; Lanson, N.; Tzogamakis, C.; Park, C. B.; Chen, P. J Phys Chem B 2007, 111, 3859.
73. Otake, K.; Kobayashi, M.; Ozaki, Y.; Yoda, S.; Takebayashi, Y.; Sugeta, T.; Nakazawa, N.; Sakai, H.; Abe, M. Langmuir 2004, 20, 6182.
74. Wu, S. J Phys Chem 1970, 74, 632.
75. Muller, M.; MacDowell, G. L.; Virnau, P.; Binder, K. J Chem Phys 2002, 117, 5480.
76. Kashchiev, D. J Chem Phys 2003, 118, 1837.